

de Vries liquid crystals based on a chiral 5-phenylpyrimidine benzoate core with a tri- and tetra-carbosilane backbone

S. P. Sreenilayam,¹ D. Rodriguez-Lojo,² D. M. Agra-Kooijman,³ J. K. Vij,^{1,*} V. P. Panov,¹ A. Panov,² M. R. Fisch,⁴ Satyendra Kumar,⁵ and P. J. Stevenson²

¹Department of Electronic and Electrical Engineering, Trinity College Dublin, The University of Dublin, Dublin 2, Ireland

²School of Chemistry and Chemical Engineering, Queens University, Belfast BT7 1NN, United Kingdom

³Liquid Crystal Institute, Kent State University, Kent, Ohio 44242, USA

⁴College of Aeronautics and Engineering, Kent State University, Kent, Ohio 44242, USA

⁵Division for Research and Department of Physics, University at Albany, New York 12222, USA



(Received 20 December 2017; published 26 February 2018)

New chiral de Vries smectic liquid-crystalline compounds are designed, synthesized, and investigated for perspective applications in defect-free bistable surface-stabilized ferroelectric liquid-crystal displays. In these compounds, a 5-phenyl-pyrimidine benzoate core is terminated on one side by a tri- or tetra-carbosilane group linked through an alkoxy group and an alkyl spacer and on the opposite side terminated by a chiral 2-octanol group. The stereogenic center contains either a methyl or perfluoromethyl functional group. These compounds exhibit Iso-SmA*-SmC*-SmX-Cr phases under cooling from the isotropic state. Measurements of the temperature-dependent smectic layer spacing by x-ray diffraction experiments combined with the measured apparent optical tilt angle and the birefringence reveal that SmA* phase in these compounds is of the de Vries type. In addition, the chiral compound with a tetra-carbosilane backbone, **DR277**, exhibits good de Vries properties with the SmC* phase exhibited over a wide temperature range. By varying the carbosilane end group, the de Vries properties are enhanced, that is, the layer shrinkage of $\sim 1.9\%$ for the tri-carbosilane **DR276** is reduced to $\sim 0.9\%$ for tetra-carbosilane **DR277** at 10°C below SmA* to SmC* transition temperature, T_{AC} . For **DR277**, the reduction factor $R \approx 0.22$ for $T = (T_{AC} - 10)^\circ\text{C}$ is reasonably low and the apparent optical tilt angle $\theta_{app} = 35.1^\circ$, hence this compound is a “good de Vries smectic” LC. Therefore, synthesis of the chiral mesogen with an even higher number of carbosilane groups may lead to a further reduction or even zero-layer shrinkage exhibited at T_{AC} with SmC* phase extending over a wide temperature range close to the room temperature for perspective suitability in device applications. Our results for 5-phenyl-pyrimidine benzoate core-based compounds support a recently drawn conclusion by Schubert *et al.* [*J. Mater. Chem. C* **4**, 8483 (2016)] from a different compound, namely that a carbosilane backbone in chiral mesogens strongly influences the de Vries properties.

DOI: 10.1103/PhysRevMaterials.2.025603

I. INTRODUCTION

Liquid-crystal (LC) devices based on ferroelectric smectics display much faster switching speeds (usually of the order of a few microseconds) compared to currently used nematic LCs where the switching speed is slow and is of the order of a few milliseconds [1]. It is therefore essential to explore ferroelectric smectics for the next generation of devices. In most chiral ferroelectric smectic LCs, an emergence of the molecular tilt at the SmA*-SmC* transition leads to a contraction of the smectic layer spacing under cooling [Fig. 1(a)]. This layer contraction combined with the surface anchoring of constituent molecules leads to an irreversible transformation of the arrangement of molecules in layers from bookshelf to chevron structures. In the latter, the layer structures fold themselves in opposite directions; these opposite folds create zigzag defects in the optical texture of a LC cell, thus degrading the quality of the devices and severely limiting their uses for a successful commercialization of ferroelectric LC displays [2–4].

An immediate solution is to avoid this problem altogether by developing new chiral LCs with a minimal layer shrinkage at the SmA*-SmC* transition temperature as well as continuing to have it within the SmC* phase [4].

The first experimental observation of smectic liquid crystals having the same layer spacing in both SmC and SmA phases was made by Diele *et al.* in Halle [5]. They also found that the layer spacing d in these materials was actually much lower than the length of the molecule L in its most extended configuration. Based on the layer-spacing results and on having determined that the SmA-SmC phase transition in these materials is of first-order, de Vries proposed that in these materials the tilt angle in the SmA phase is not zero contrary to conventional assumption made [Fig. 1(a)] until that time [6]. This unusual behavior was originally explained by the diffuse cone model [Fig. 1(b)] in which molecules in the SmA phase have a tilted orientation and these tilt directions are disordered in azimuthal (φ) angle [7,8]. According to this model, the SmA-SmC phase transition is affected by ordering of φ to a specific tilt direction with a certain value. This explains why the SmA-SmC transition is first-order with zero-layer contraction. These observations were made when most smectic LCs were formed from

*Author to whom all correspondence should be addressed: jvij@tcd.ie

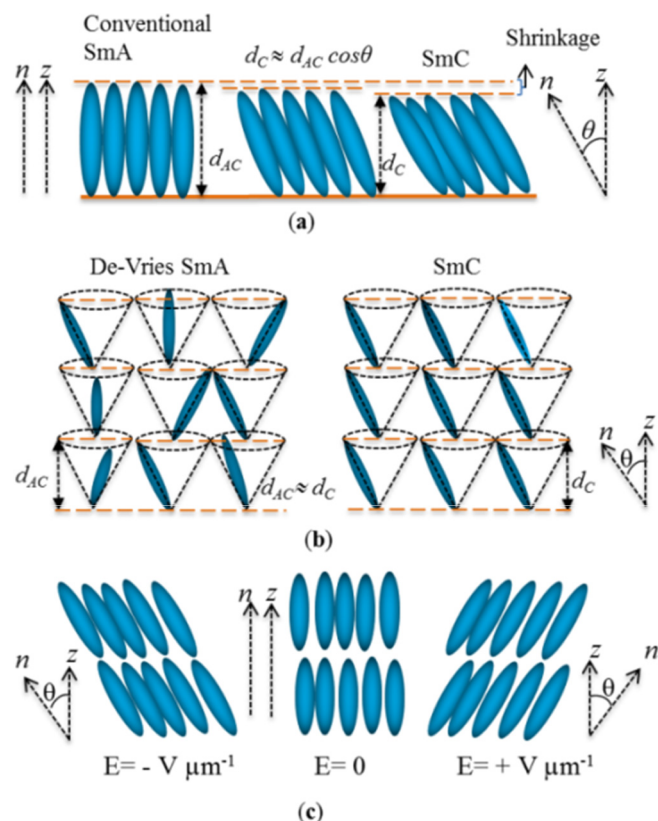


FIG. 1. Schematic representation of the molecular arrangements in SmA and SmC phases in accordance with (a) a conventional model for the smectic A and C phases, (b) the de Vries diffuse-cone model, and (c) a demonstration of the electroclinic effect in a SmA* phase. z is the layer normal, n is the average direction of the molecular long axis orientation, θ is the angle between n and z , d_C and d_A are the layer spacings in SmC and SmA, whereas d_{AC} is the layer spacing at the SmA to SmC phase transition temperature T_{AC} .

achiral molecules. If we introduce chirality, then these phases are denoted by SmA* and SmC*. This special class of chiral smectics possesses a large field-induced electroclinic effect (linear dependence of the induced apparent tilt angle θ_{app} on a weak applied electric field E) [9,10] [Fig. 1(c)], large molecular fluctuations especially in the tilt [11–13], and a significantly large increase in the birefringence with the electric field, especially close to the SmA*-SmC* transition temperature [14,15].

Several chiral and nonchiral LC materials have recently been found to exhibit maximum layer shrinkage ranging from 0.2% to 1.7% [10,16–22], or in some cases extremely low layer shrinkage at the SmA-SmC transition is displayed [14]. Among the siloxane-terminated nonchiral materials, mesogen **3(n)** [Fig. 2(a)] shows good de Vries-like properties [19] and undergoes a SmA to SmC phase transition with a layer shrinkage ranging from 0.5% to 1.4%, which is rather low. The tri-carbosilane **QL32-6**, a chiral analog of mesogen **3(n)**, shows a low-layer contraction of only 0.2% upon the phase transition from the uniaxial SmA* to the tilted SmC* phase [18]. The siloxane-terminated **TSiKN65** [15] [Fig. 2(b)] and its carbosilane analog **W599** [23] [Fig. 2(b)] are among the best chiral de Vries LCs reported to date since these materials undergo a first-order SmA* to SmC* phase transition upon cooling, where the layer shrinkage is <1%. The transition is

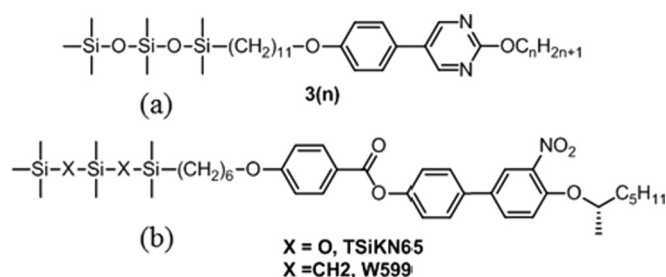


FIG. 2. Molecular structures of (a) **3(n)** [19] and (b) **TSiKN65/W599** [15,23].

accompanied by a large increase in the birefringence with applied electric field. Also, these compounds exhibit remarkably high electroclinic susceptibilities, i.e., the apparent tilt angles for electric fields $<5 \text{ V}/\mu\text{m}$ and for $(T - T_{AC}) = +1^\circ\text{C}$ are 31° and 25° , respectively. These compounds are based on a nitro biphenyl benzoate core, terminated by a chiral alkoxy chain on one side and by the siloxane or carbosilane alkoxy chain on the opposite side [Fig. 2(b)].

With these structures in mind, we have designed a series of compounds with a 5-phenylpyrimidine benzoate core (Fig. 3) to explore the properties of mesogens that combine functional groups present in some of the most remarkable de Vries materials but with a different core of the mesogen [19,15,23]. The studied molecules are structurally related to each other. These have the same aromatic core and carbosilane backbone on one side. In particular, it is found that the carbosilane group promotes SmC behavior, whereas 5-phenylpyrimidine promotes SmA. The latter can generally be regarded as the SmA promoting element. Carbosilane-based materials **ADPD003** and **DR253** are terminated by an alkoxy chain involving chiral CF_3 on the opposite end of the core. However, in **DR276** and **DR277**, the CF_3 group is replaced by the CH_3 group. The only difference between **DR277** and the tricarbosilane **DR276** is the addition of one more carbosilane group, i.e., it contains a tetra-carbosilane backbone. An ester group in the mesogen core increases the polarity of the molecule, and the chiral center is responsible for inducing chiral smectic phases. The transition temperatures with the enthalpy of transitions and phases of the studied compounds using differential scanning calorimetry (DSC) are given in Table I.

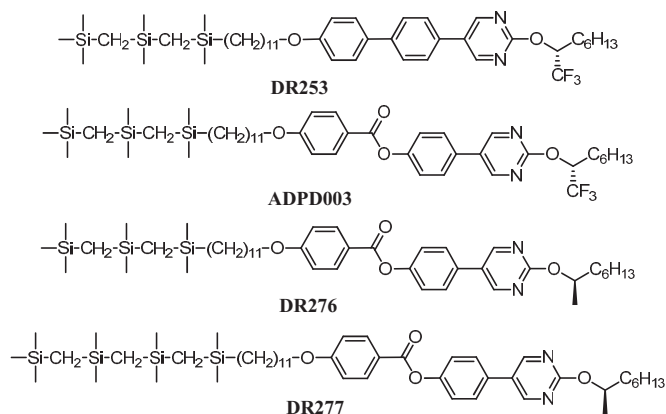


FIG. 3. Molecular structure and names of the compounds under investigation.

TABLE I. Mesophases with transition temperatures that have been determined experimentally as stated in the text. Transition enthalpies ΔH (in J/g) are detected upon second cooling carried out at the rate of $10^\circ\text{C min}^{-1}$ by differential scanning calorimetry (DSC). Mesophase transitions are also investigated using a polarizing optical microscope (POM). Iso and Cr denote the isotropic liquid and the solid crystal states, respectively. The negative value within the parenthesis is the enthalpy change in J/g obtained by DSC under cooling.

LC Material	Mesophases and transition temperatures with transition enthalpies (ΔH in J/g) under cooling
DR253	Cr 50.2°C (-15.3) Iso
ADPD003	Cr 52°C (-26.7) Iso
DR276	Cr 14°C (-23.7) SmX 48°C ($-$) SmC* 78.5°C (-0.4) SmA* 87°C (-2.7) Iso
DR277	Cr 6°C (-17.3) SmX 35°C ($-$) SmC* 65.5°C (-0.4) SmA* 77°C (-1.1) Iso

The main objective of this study is to develop de Vries LCs for bistable surface-stabilized ferroelectric liquid-crystal (SSFLC) displays that exhibit defect-free behavior. These are made possible by investigating the de Vries properties while systematically varying the length of the carbosilane tail. In the de Vries scenario, the LC molecules in the SmA* phase are already tilted in the absence of electric field. Application of the electric field only orders the azimuthal directions of the tilt, such that in doing so, the field does not induce any layer contraction and thereby avoids chevron defects from appearing in the optical texture. In this work, we report on the design, synthesis, and characterization of carbosilane-terminated smectic materials, denoted as **DR253**, **ADPD003**, **DR276**, and **DR277**. The molecular design involves two elements: (i) a carbosilane tail, which promotes SmC, and (ii) 5-phenylpyrimidine, which promotes SmA. Liquid-crystalline phase transitions are investigated by using DSC, polarized optical microscopy (POM), and x-ray diffraction (XRD). The electro-optical studies include the results of birefringence and the apparent tilt angle. In this paper, we investigate ferroelectric properties, the electroclinic effect, and the corresponding “de Vries-like” behavior in the carbosilane-terminated **DR276** and **DR277** mesogens. Mulligan *et al.* studied the effect of varying the length of the carbosilane end group on the de Vries properties of nonchiral LCs with chloroterminated alkoxy chains [22]. They reported that the de Vries properties in 5 phenyl-1,3,4-thiadiazole achiral mesogen are enhanced by an increase in the length of the end group: from monocarbosilane to tricarbosilane. To the best of our knowledge, no other compounds have been reported in the literature so far involving a further increase in the carbosilane chain length from the tricarbosilane tail. Therefore, for drawing a comparison we

have synthesized chiral materials with tri- and tetra-carbosilane attachments, and these are studied here in detail. Herein, we discuss the effect of varying the length of the carbosilane tail from tri- to tetra- on the de Vries properties in the chiral 5-phenylpyrimidinebenzoate mesogen. The tetra-carbosilane-terminated mesogen **DR277** undergoes SmA*-SmC* transition with a maximum layer contraction of only 0.9% in the SmC* phase and a reduction factor R of ~ 0.222 relative to its thickness at the SmA*-SmC* transition temperature, T_{AC} . These parameters suggest that **DR277** is one of the best chiral de Vries smectics synthesized so far with a wide temperature range of smectic A* and C* phases and specifically SmC* occurring close to the room temperature.

II. EXPERIMENT

A. Material synthesis

The chiral mesogen **DR253** was formed following the synthetic approach as shown in Fig. 4. Nucleophilic aromatic substitution of 5-bromo-2-chloropyrimidine with a fluorinated chiral alcohol gave **1**. 11-Bromoundec-1-ene was hydrosilylated with ((dimethylsilyl)methyl)-dimethyl((trimethylsilyl)methyl)silane (prepared as described) [24] under standard conditions using Karstedt's catalyst to form a silyl-terminated bromide chain. An S_N2 substitution of the silylated bromide with 4-bromo-4'-hydroxybiphenyl in basic media led to compound **2** in 82% yield. From this boronic acid, **3** was formed from **2** using standard conditions of $t\text{BuLi}$ and trimethylborate at -78°C . A Suzuki cross coupling was used to combine the fragments **1** and **3** leading to **DR253** in 51% yield.

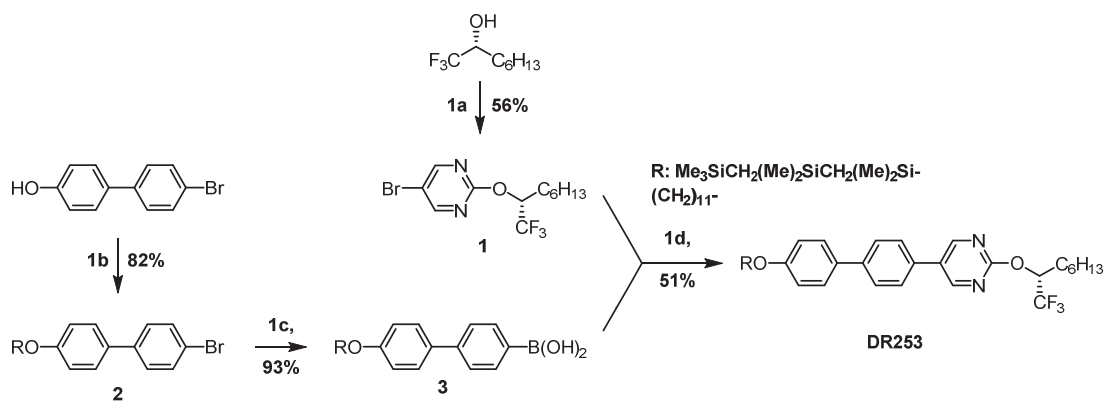


FIG. 4. Reagents and conditions: (1a) Na, toluene, 50°C ; (1b) $\text{Me}_3\text{SiCH}_2(\text{Me})_2\text{SiCH}_2(\text{Me})_2\text{Si}-(\text{CH}_2)_{11}-\text{Br}$, K_2CO_3 , DMF, 80°C ; (1c) $t\text{BuLi}$, $\text{B}(\text{OMe})_3$, THF, -78°C ; (1d) $\text{Pd}(\text{PPh}_3)_4$, $\text{K}_2\text{CO}_3(\text{aq})$, toluene/MeOH, reflux.

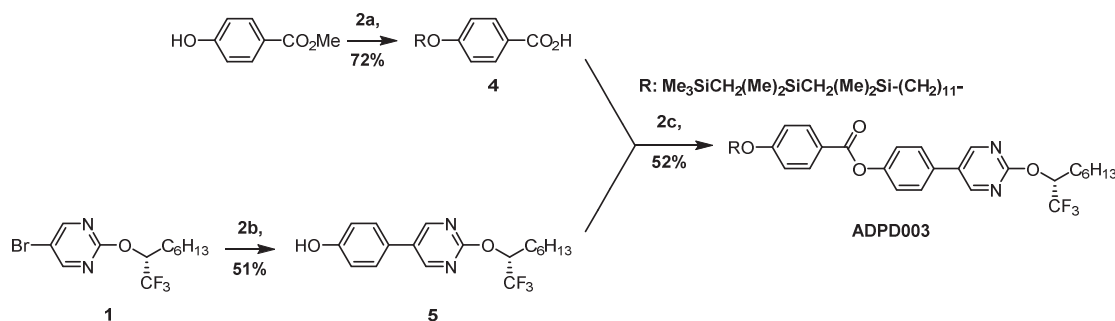


FIG. 5. Reagents and conditions: (2a) 1.) $\text{Me}_3\text{SiCH}_2(\text{Me})_2\text{SiCH}_2(\text{Me})_2\text{Si}-(\text{CH}_2)_{11}-\text{Br}$, K_2CO_3 , DMF; 2.) NaOH, EtOH/ H_2O , reflux; (2b) 4-hydroxyphenylboronic acid, $\text{Pd}(\text{PPh}_3)_4$, $\text{K}_2\text{CO}_3(\text{aq})$, toluene/MeOH, reflux; (2c) DCC, DMAP, DCM.

The chiral mesogen **ADPD003** was prepared following the synthetic approach shown in Fig. 5. The aforementioned silyl-terminated bromide was substituted with methyl 4-hydroxybenzoate in basic media. The ester was then hydrolyzed using sodium hydroxide under reflux giving acid **4** in 72% yield over the two steps. Suzuki cross coupling of 4-hydroxyphenylboronic acid with aryl bromide **1** gave product **5** in 51% yield. The acid **4** and phenol **5** were condensed using *N,N'*-dicyclohexylcarbodiimide (DCC) to give the final product in 52% yield.

The compounds **DR276** and **DR277** were prepared following the synthetic approach shown in Fig. 6. The first step was an S_N2 displacement of 11-bromoundec-1-ene with ethyl 4-hydroxybenzoate in basic media followed by treatment with LiOH in MeOH/ H_2O , which led to the carboxylic acid **6** in 86% yield. Suzuki cross coupling of (4-hydroxyphenyl)boronic acid and pyrimidine ether **7** gave pyrimidine **8** in 59% yield. Coupling of **6** and **8** using DCC and 4-Dimethylaminopyridine (DMAP) in Dichloromethane (DCM) led to the ester **9** in 82% yield. **DR276** was prepared by hydrosilylation of the alkene **9** using ((dimethylsilyl)methyl)dimethyl-((trimethylsilyl)methyl)silane and platinum(0)-1,3-divinyl-1,1,3,3-tetramethyldisiloxane as a catalyst in 56% yield. The same conditions were used for **DR277** except the silane used was 2,2,4,4,6,6,8,8-heptamethyl-2,4,6,8-tetrasilanonane in 43% yield.

B. Experimental techniques and measurements: Calorimetry, electro-optical studies, and x-ray diffraction

Differential scanning calorimetry (Perkin-Elmer DSC-7 calorimeter) is initially used to characterize the smectic LCs

studied here, where the phase transition is investigated by the enthalpy change at the transition temperature(s). Using this technique, we can effectively measure a change in the heat capacity of a material as a function of temperature by comparing it with a standard reference material. Measurements are carried out under both cooling and heating cycles at a rate of $10^\circ\text{C min}^{-1}$. It is emphasized here that a heating and cooling rate of $10^\circ\text{C min}^{-1}$ is actually a fairly fast scanning rate, and for this reason alone the results of very small enthalpies of transitions may be somewhat inaccurate. Furthermore, this may also introduce significant hysteresis in transition temperatures between the cooling and heating runs.

The electro-optical studies are carried out on planar-aligned cells with a parallel rubbed polyimide alignment layer KSRP-XX/D611P6NSS05 purchased from EHC, Japan. The LC cells are studied using an Olympus BX 52 polarizing optical microscope (POM) equipped with a hot stage. The latter is connected to a temperature controller, Eurotherm 2604.

X-ray diffraction (XRD) experiments were carried out using a Rigaku Screen Machine. This unit has a microfocus sealed x-ray tube with a copper anode that generates x rays at a wavelength of $\lambda = 1.5418 \text{ \AA}$. X rays are incident on the sample contained in a flamed sealed quartz capillary (1.0 mm diam, wall thickness 0.01 mm), and the diffracted x-ray patterns are recorded by a Mercury 3 CCD detector with a resolution of 1024×1024 pixels, with a pixel size of $73.2 \mu\text{m} \times 73.2 \mu\text{m}$. The detector was positioned at a distance of approximately 77 mm from the sample to cover the observable length scale characteristics of the molecular system with dimensions ranging from 3.4 to 60 \AA . The sample capillary was mounted in a Linkam HFS350-CAP hot stage with a temperature-controlled

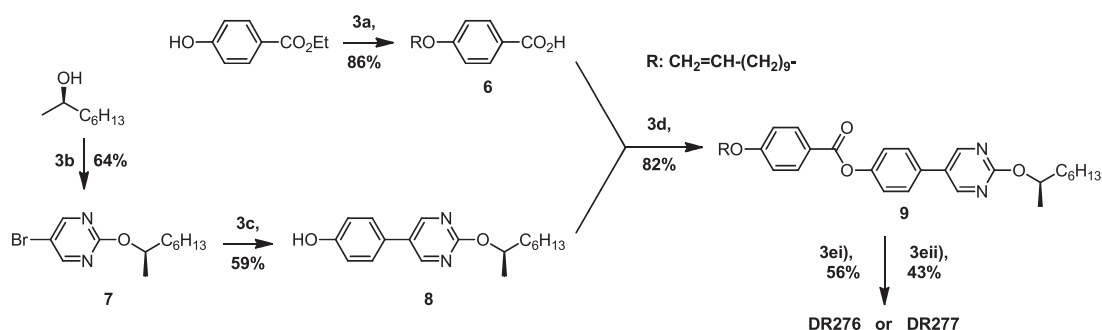


FIG. 6. Reagents and conditions: (3a) 1.) 11-bromoundec-1-ene, K_2CO_3 , DMF; 2.) LiOH, MeOH/ H_2O , reflux; (3b) Na, toluene, 55°C ; (3c) (4-hydroxyphenyl)boronic acid, $\text{Pd}(\text{PPh}_3)_4$, $\text{K}_2\text{CO}_3(\text{aq})$, toluene/MeOH, reflux; (3d) DCC, DMAP, DCM; (3ei) Karstedt's catalyst, $\text{Me}_3\text{SiCH}_2(\text{Me})_2\text{SiCH}_2(\text{Me})_2\text{SiH}$, THF; (3eii) Karstedt's catalyst, $\text{Me}_3\text{SiCH}_2(\text{Me})_2\text{SiCH}_2(\text{Me})_2\text{SiCH}_2(\text{Me})_2\text{SiH}$, THF.

oven with a temperature stability of $\pm 0.05^\circ\text{C}$. A built-in pair of samarium cobalt rare-earth magnets was placed between the capillary mount to aid the orientation of the LC molecules. The sample temperature was controlled with the LINKSYS32 software [25] installed in the computer system used for data collection. All scans were calibrated against a Silver Behenate standard, and the background scattering is subtracted (scattering from the empty capillary in the same sample position) before the data were analyzed with the aid of FIT2D software [26] and MATHEMATICA. Smectic layer spacing was determined from the position of the main Bragg reflection peaks.

III. RESULTS AND DISCUSSION

A. Differential scanning calorimetry and polarizing optical microscopy

The DSC thermograms of compounds **DR253** [see Fig. S1(a) in the Supplemental Material [44]] and **ADPD003** [see Fig. S1(b) in the Supplemental Material [44]] are shown to exhibit first-order transitions on cooling from the isotropic

liquid to the crystalline state with enthalpy change (ΔH) of -50 J g^{-1} at 52°C and -26.4 J g^{-1} at 52°C , respectively. The phases and the transition temperatures are confirmed using a polarizing optical microscope (POM) (see Figs. S2 and S3 in the Supplemental Material [44]).

Figure 7(a) shows the DSC thermogram of the material **DR276**, 5-phenyl-pyrimidine benzoate core, terminated on one side by a tri-carbosilane backbone and on the opposite by the chiral alkyloxy chain involving the CH_3 group. Upon cooling the sample from the isotropic to SmA^* , a first-order phase transition is observed at a temperature of $\sim 87^\circ\text{C}$ with an enthalpy (ΔH) change of $\sim -2.7\text{ J g}^{-1}$. The SmA^* phase was characterized by the observations of a focal conic fan-shaped texture in a $9\text{ }\mu\text{m}$ planar-aligned cell in a POM [Fig. 7(c)], and an optically uniaxial dark texture is seen in a $4.3\text{ }\mu\text{m}$ homeotropically aligned cell [Fig. 7(f)] under a POM [27]. Upon a further reduction of temperature, the material undergoes a weakly first-order SmA^* to SmC^* phase transition at a temperature $\sim 78.5^\circ\text{C}$ with a transition enthalpy $\Delta H \sim -0.4\text{ J g}^{-1}$. The POM textures for the phase transition are

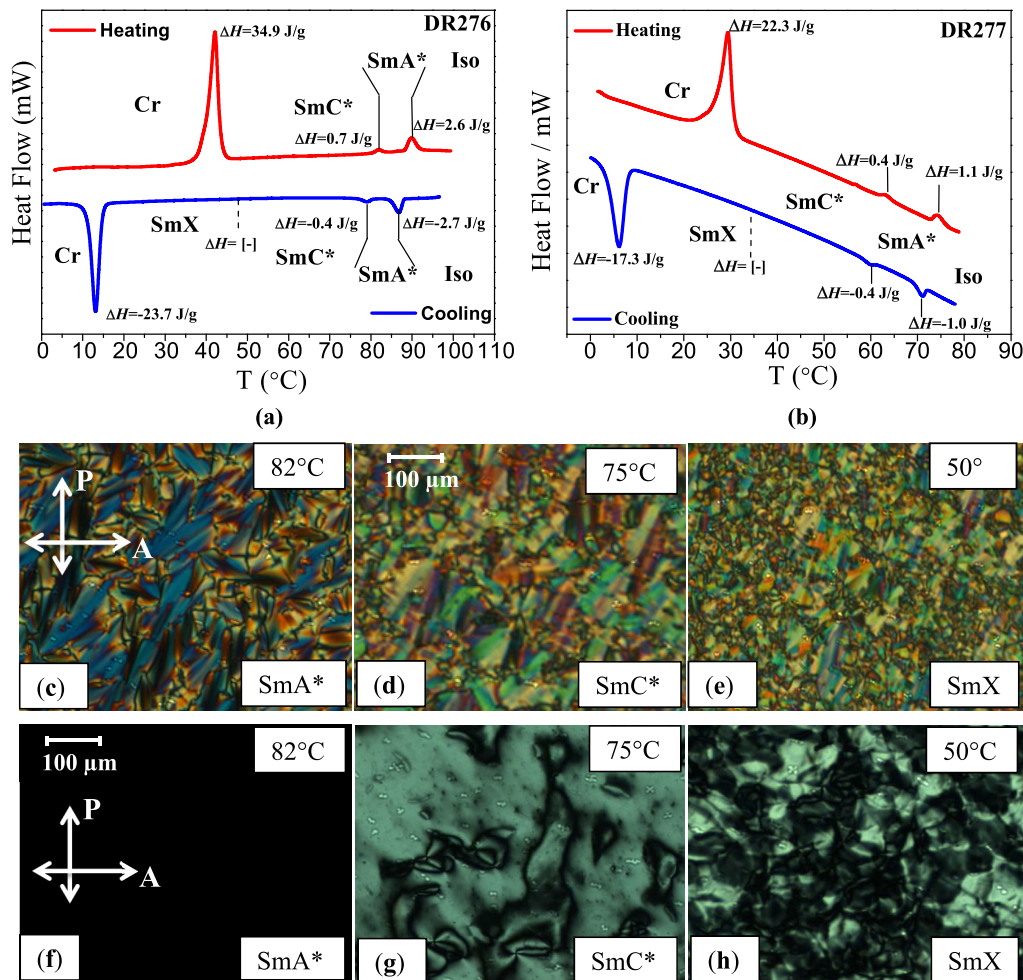


FIG. 7. Differential scanning thermograms (DSC) of (a) **DR276** and (b) **DR277**. The first cooling and second heating thermograms are obtained by ramping the temperature at a rate of $10^\circ\text{C min}^{-1}$; continuous mesophase transitions without visible enthalpy are indicated by dashed lines. The POM images of mesophases observed in **DR276**; (c)–(h) under crossed polarized conditions, textures are recorded as (c)–(e) for a planar-aligned cell (of thickness $d = 9\text{ }\mu\text{m}$) and as (f)–(h) for a homeotropically aligned cell ($d = 4.3\text{ }\mu\text{m}$). Textures are recorded under cooling cycles, (c) and (f) SmA^* phase at 82°C ; (d) and (g) SmC^* phase at 75°C ; and (e) and (h) SmX phase at 50°C ; SmX is not characterized/identified here.

shown in Figs. 7(d) and 7(g). The SmC^* phase is distinguished from SmA^* by the observation of a change in the optical texture [28]. The fan-shaped texture characteristic of SmA^* on cooling to the SmC^* leads to the broken fan-shaped texture seen in Fig. 7(d) in a planar-aligned cell; the latter texture is characteristic of SmC^* . The dark texture of SmA^* in a homeotropically aligned cell arises as LC molecules are oriented normal to the substrates; this changes to a Schlieren texture upon a transition from SmA^* to SmC^* [Fig. 7(g)]. For a conventional SmA^* - SmC^* phase transition, the tilt angle remains at the zero value in SmA^* phase down to the transition temperature T_{AC} , the DSC thermogram usually exhibits a second-order transition with a step in the baseline without showing a peak for the enthalpy of the transition, however a change in the heat capacity is observed [29]. Upon lowering the temperature again, a monotropic SmX is formed, distinguished by a POM texture of a homeotropically aligned cell [Fig. 7(h)]. In a DSC thermogram, a SmA^* to SmX phase transition is observed to be of second order without showing any enthalpy at the transition [see Figs. 7(a) and 7(b)].

A representative DSC plot of **DR277**, in which a 5-phenylpyrimidine benzoate core is terminated by tetra-carbosilane on

one side and on the opposite side by a chiral alkyloxy chain with a CH_3 group (structure given in Fig. 3), is shown in Fig. 7(b). This undercooling exhibits three transition peaks. Similar to the tricarbosilane **DR276**, this tetra-carbosilane smectic shows a first-order isotropic to SmA^* transition with $\Delta H \sim -1.0 \text{ J g}^{-1}$ at a temperature of $\sim 77^\circ\text{C}$. Upon lowering the temperature, the compound undergoes a weakly first-order SmA^* to SmC^* transition with ΔH of $\sim -0.4 \text{ J g}^{-1}$ at 65.5°C . Phases SmA^* and SmC^* that correspond to within the transition peaks are confirmed in planar-aligned ($d = 9 \mu\text{m}$) and homeotropically aligned ($d = 4.3 \mu\text{m}$) cells using a POM (see Figs. S4a and S4b and Figs. S5a and S5b in the Supplemental Material [44]). Also, the monotropic SmX phase (see Figs. S4c and S5c in the Supplemental Material [44]) exhibits a second-order transition without showing any enthalpy change.

During heating cycles, both compounds **DR276** and **DR277** display a SmC^* phase that upon further heating transforms to SmA^* and then finally changes to the isotropic state. As shown in Figs. 7(a) and 7(b), increasing the length of the carbosilane backbone results in a gradual widening of the temperature range of SmA^* phase. The tri-carbosilane **DR276** having an $\sim 8.5^\circ\text{C}$ -wide SmA^* phase shows a first-order crystallization

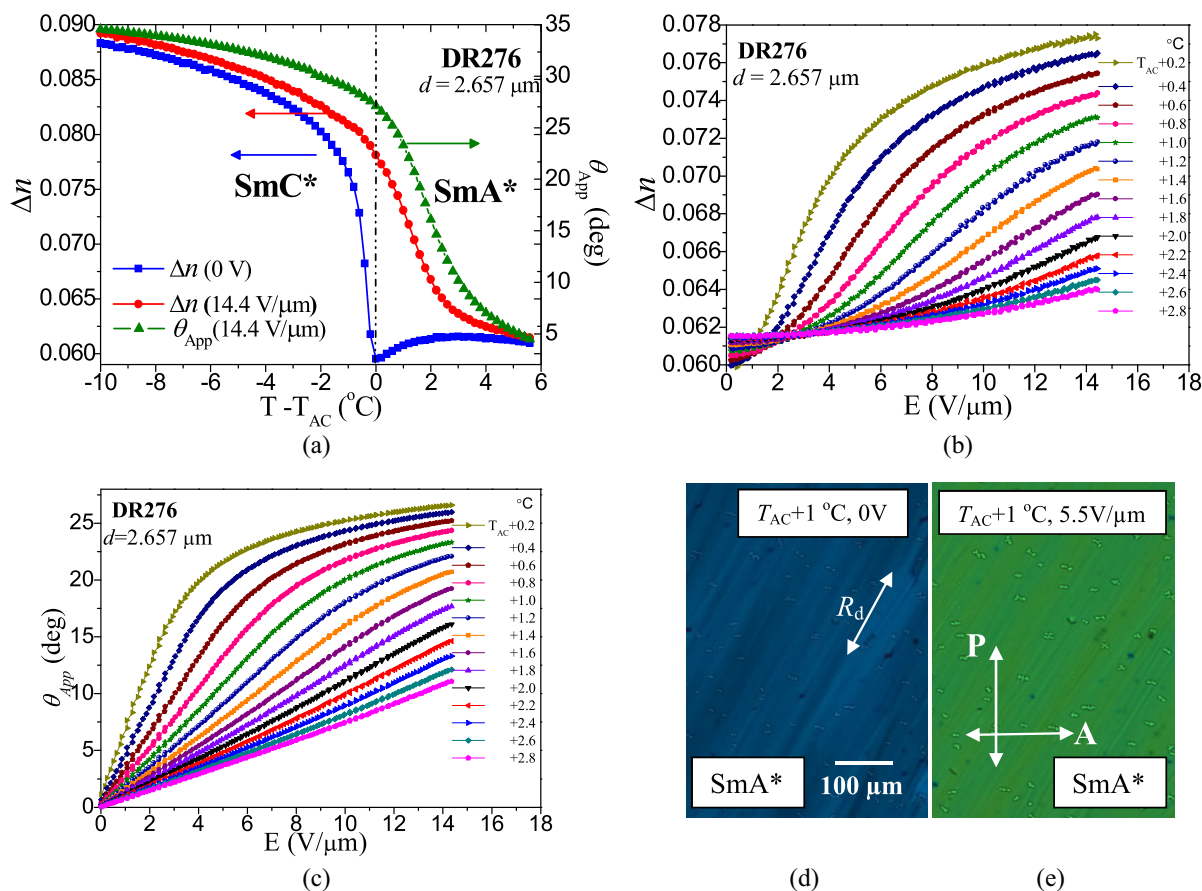


FIG. 8. Plots for the measured values of birefringence, Δn , and the apparent optical tilt angle, θ_{app} , for **DR276** in a $2.657 \mu\text{m}$ planar-aligned cell as a function of (a) temperature in the absence of the field and at an ac field of $14.4 \text{ V}/\mu\text{m}$ ($f = 81.7 \text{ Hz}$) in the SmA^* and SmC^* phases. The frequency is low enough that it is regarded to be close to dc but it high enough to prevent ions from contributing to the results. (b) Δn and (c) θ_{app} for selected temperatures in the SmA^* phase. Parts (d) and (e) are the POM textures of the SmA^* phase for 0 V and $5.5 \text{ V}/\mu\text{m}$ at 1°C ($T_{AC} + 1^\circ\text{C}$) above the SmA^* to SmC^* phase-transition temperature T_{AC} . Texture observations of a $9 \mu\text{m}$ planar-aligned cell under crossed polarizers are carried out by using a 110 Hz square wave AC signal and by keeping the rubbing direction at an angle of $\alpha = 23^\circ$ to the polarizer/analyzer position.

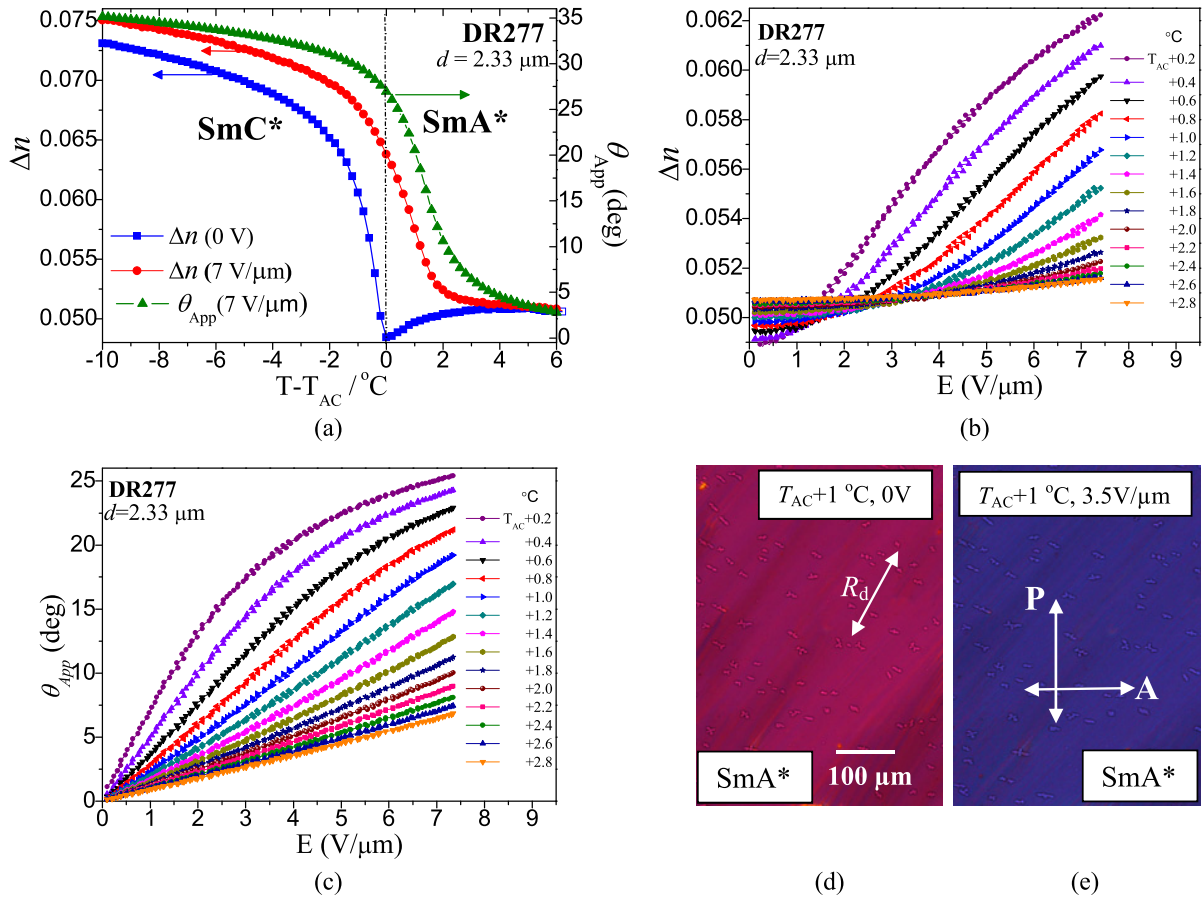


FIG. 9. Plots of Δn and θ_{app} determined as indicated for **DR277** in a planar-aligned cell of cell thickness $2.33 \mu\text{m}$. (a) Temperature dependences of Δn at 0 V , Δn at $7 \text{ V}/\mu\text{m}$, and θ_{app} at $7 \text{ V}/\mu\text{m}$ ($f = 44 \text{ Hz}$) in the SmA* and SmC* phases. Electric field ($f = 44 \text{ Hz}$) dependences of (b) Δn and (c) θ_{app} for selected temperatures in the SmA* phase. Parts (d) and (e) are the POM textures of the SmA* phase for 0 V and $3.5 \text{ V}/\mu\text{m}$ at 1°C ($T_{AC} + 1^\circ\text{C}$) above the SmA* to SmC* phase-transition temperature T_{AC} . Texture observations under crossed polarizers are made in a planar-aligned cell of cell thickness $9 \mu\text{m}$ by using 110 Hz square wave ac voltage and keeping the rubbing direction at an angle of $\alpha = 23^\circ$ to the polarizer/analyzer position.

transition with ΔH of $\sim -23.7 \text{ J g}^{-1}$ at a temperature of $\sim 14^\circ\text{C}$ [Fig. 7(a)]. However, an addition of one more carbosilane group in **DR277** further widens the temperature range of SmA* to $\sim 12.5^\circ\text{C}$ and the crystallization transition temperature is lowered to $\sim 6^\circ\text{C}$ with $\Delta H = \sim -17.3 \text{ J g}^{-1}$ [Fig. 7(b)].

B. The measurements of birefringence (Δn), apparent tilt angle (θ_{app}), and the polarization (P_s)

Birefringence (Δn) and the apparent optical tilt angle (θ_{app}) measurements are conducted on planar-aligned cells of **DR276** [results shown in Figs. 8(a)–8(c)] and **DR277** [results shown in Figs. 9(a)–9(c)] LCs, having cell thicknesses of $d = 2.67$ and $2.33 \mu\text{m}$, respectively. Δn and θ_{app} are measured by recording the transmitted light while varying the orientations of the polarizer and the analyzer [30]. The experiment is performed by applying a triangular signal of $14.4 \text{ V}_{0-pk} \mu\text{m}^{-1}$ ($f = 81.7 \text{ Hz}$) for **DR276** [Figs. 8(a)–8(c)] and $7 \text{ V}_{0-pk} \mu\text{m}^{-1}$ ($f = 44 \text{ Hz}$) for **DR277** [Figs. 9(a)–9(c)]. Frequencies of the applied signal are chosen to be low enough in order to allow for a sufficient time for electro-optical switching to occur while at the same time it is high enough to avoid the ionic conductivity

to make a contribution to the switching current. The amplitude of the voltage applied to a planar-aligned cell of **DR276** is large enough to make θ_{app} increase slowly at first but eventually to saturate with the maximum applied electric field [Figs. 8(b) and 8(c)]. However, for **DR277** the applied electric field is not large enough to saturate θ_{app} completely [Figs. 9(b) and 9(c)].

Figure 8(a) shows the temperature dependence of Δn for **DR276** at zero field as well as for a maximum applied field of $14.4 \text{ V } \mu\text{m}^{-1}$. Upon cooling the planar-aligned cell of **DR276**, the magnitude of the zero-field birefringence, Δn , decreases within the SmA* phase with a reduction in temperature and especially dramatically closer to the SmA*-SmC* transition temperature T_{AC} ($\Delta n = \sim 0.059$). This behavior is different from that of a conventional SmA* phase where Δn increases with decreasing temperature due to an increase in the orientational order parameter. Thus, the tilt angle of the molecules in the conventional SmA* phase changes little with temperature and field close to the transition temperature. A continuous disorder in the azimuthal angle with increasing molecular tilt with a reduction in temperature results in Δn decreasing as temperature is lowered. As the temperature approaches the SmA*-SmC* phase transition T_{AC} , the zero-field Δn suddenly increases in the SmC* followed by a slow increase with a

reduction in temperature within the SmC^* phase itself. This is because the azimuthal angles are ordered close to the transition, but the optical tilt starts increasing with a further reduction in temperature. The temperature dependence of Δn with an applied electric field ($14.4 \text{ V}/\mu\text{m}$) across a planar-aligned cell shows behavior in the SmA^* phase that is entirely different from its zero-field value [Fig. 8(a)]. The magnitude of Δn in the entire temperature range of the SmA^* phase [Figs. 8(a) and 8(b)] now increases continuously. This is affected by reorienting the molecular azimuthal tilts through breaking the degeneracy in the azimuthal angle. An emergence of the optical tilt leads to a substantial increase in Δn with field. Thus, the observed behavior is consistent with the diffuse-cone model of the SmA^* with a first-order SmA^* - SmC^* phase-transition temperature [Fig. 7(a)]. This field-induced increase in Δn in the SmA^* phase is in agreement with a change in the interference colors recorded by the POM at a temperature of 79.5°C , approximately 7.5°C below the Iso- SmA^* transition temperature and 1°C above T_{AC} [Figs. 8(d) and 8(e)]. POM textures of a planar-aligned cell of thickness $9 \mu\text{m}$, shown in Figs. 8(d) and 8(e), are recorded by fixing the rubbing direction \mathbf{R}_d at an angle of $\alpha \approx 23^\circ$ to the polarizer/analyzer direction. When placed between the crossed polarizer/analyzer, a SmA^* phase at 79.5°C in the planar-aligned cell shows a uniform dark blue color due to a finite value of Δn [Fig. 8(d)]. An application of the external electric field, $5.5 \text{ V}/\mu\text{m}^{-1}$ across the planar-aligned cell, shows a significant change in the color of the texture as a result of the increase in the birefringence. This is shown in Fig. 8(e).

Temperature dependences of θ_{app} in the SmA^* and SmC^* phases of **DR276** for a maximum applied field of $14.4 \text{ V}/\mu\text{m}^{-1}$ are plotted in Fig. 8(a) (green triangles). The dependences of Δn (E) on temperature are also given [red circles in Fig. 8(a)]. Such a coupling between θ_{app} and Δn , first proposed by Lagerwall *et al.* [31], is being demonstrated here. The dependence of θ_{app} on E is plotted in Fig. 8(c) in the SmA^* phase of **DR276**. The data are shown for a few temperatures only in order to avoid the figure being overcrowded. At higher temperatures in the SmA^* phase where θ_{app} is low, a linear increase in θ_{app} with electric field is observed. However, in the vicinity of the SmA^* - SmC^* transition temperature, the electroclinic response is seen to increase dramatically and a nonlinearity in θ_{app} with E is recorded especially for $\theta_{\text{app}} > 15^\circ$. In the SmA^* phase, close to the transition temperature T_{AC} , θ_{app} rises rapidly with the applied electric field to a value of $\sim 23^\circ$ and then it increases more slowly with increasing field, finally reaching almost saturation at 26.5° for a field of $14.4 \text{ V}/\mu\text{m}^{-1}$.

Figure 9(a) shows the temperature dependence of Δn for a planar-aligned cell of **DR277** for (i) the absence of an electric field and (ii) a maximum applied E of $7 \text{ V}/\mu\text{m}^{-1}$. Similar to the behavior of **DR276**, the magnitude of zero-field Δn for **DR277** is also shown to decrease within the SmA^* phase upon cooling, where a much larger drop closer to the SmA^* - SmC^* transition temperature T_{AC} is recorded. A comparison of the zero-field Δn values in the SmA^* phase of **DR277** (zero-field Δn at $T_{\text{AC}} = \sim 0.048$) shows a relatively lower magnitude than for trisiloxane **DR277** (zero-field Δn at $T_{\text{AC}} = \sim 0.059$). This may be due to the presence of more bulky siloxane groups in **DR277** than in **DR276**. Since the siloxane groups are more flexible and may exhibit more irregular conformations [15] than a bunch

of hydrocarbon groups, the magnitude of Δn for both **DR276** and **DR277** in planar-aligned cells is relatively low, but more so for the latter. This may be due to the shape anisotropy of the LC molecules, and as a consequence it increases the onset of crystallinity to a higher temperature in **DR276** compared to **DR277**. This is observed in Figs. 7(a) and 7(b).

The temperature and the electric-field dependences of θ_{app} of **DR277** are shown in Figs. 9(a) and 9(c). Upon the application of a $7 \text{ V}/\mu\text{m}^{-1}$ electric field in the SmA^* phase, θ_{app} shows an increasing trend with a reduction in temperature, and the magnitude of θ_{app} at $(T_{\text{AC}} + 0.2)^\circ\text{C}$ is $\sim 26.1^\circ$ [Fig. 9(a)]. At higher temperatures in the SmA^* phase, we find an expected linear increase in θ_{app} with applied field [Fig. 9(c)], and the electroclinic response becomes nonlinear closer to T_{AC} . Here, the applied $7 \text{ V}/\mu\text{m}^{-1}$ electric field is not large enough to saturate θ_{app} even at the lower-temperature range of the SmA^* phase. $7 \text{ V}/\mu\text{m}^{-1}$ is the maximum field that can be applied to the sample without the material deteriorating.

The POM images of a planar-aligned cell of thickness $9 \mu\text{m}$ containing **DR277** recorded at 65.5°C ($\sim 11.5^\circ\text{C}$ below the isotropic to SmA^* transition temperature and 1°C above T_{AC}) are shown in Fig. 9(d). For texture observations, the cell is fixed in the hot stage by keeping the LC cell rubbing direction \mathbf{R}_d at an angle $\alpha = \sim 23^\circ$ to the polarizer/analyzer. Like **DR276**, the electric-field treatment at higher temperatures of **DR277** in the SmA^* phase closer to the isotropic phase generates a uniform monodomain alignment. This is reasonably satisfactory for carrying out the electro-optical studies (Fig. 9). Under crossed polarizers, the SmA^* phase shows a uniform pink birefringence color due to a finite value of Δn [Fig. 9(d)], and application of an external field, $7 \text{ V}/\mu\text{m}^{-1}$, produces an obvious change in the color of the POM texture [Fig. 9(e)], indicating an increase in the magnitude of Δn [Figs. 9(a) and 9(b)].

In the conventional SmA^* phase, LC molecules have strong orientational order even at zero electric field. Therefore, the magnitude of Δn in the absence of an electric field is usually large, and upon the application of a field, molecules stay parallel to each other in a planar-aligned cell, hence the field dependent variation of Δn is very weak. By contrast, in de Vries

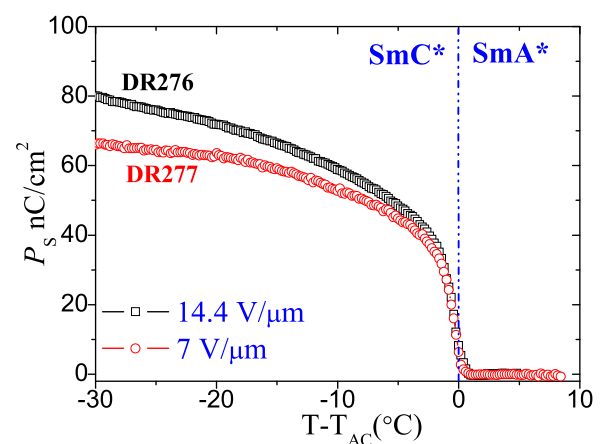


FIG. 10. Spontaneous polarization P_S vs $(T - T_{\text{AC}})$ for **DR276** (\square , $d = 2.657 \mu\text{m}$, $E = 14.4 \text{ V}/\mu\text{m}$, $f = 81.7 \text{ Hz}$) and **DR277** (\circ , $d = 2.33 \mu\text{m}$, $E = 7 \text{ V}/\mu\text{m}$, $f = 44 \text{ Hz}$). Measurements are carried out on planar-aligned cells under cooling by the application of triangular wave ac voltage.

SmA^* , the LC molecules are orientationally distributed about a tilt cone in the absence of the external electric field. Therefore, upon lowering the temperature from the high-temperature side of the SmA^* phase to the SmA^* - SmC^* transition temperature, T_{AC} , the zero-field Δn is greatly reduced due to the orientational averaging of molecules about the tilt cone. Upon the application of an electric field, the azimuthal tilt direction becomes biased and the azimuthal angles condense to a specific value. As a result, Δn of the de Vries SmA^* phase should increase substantially with applied field. In the materials under study, θ_{app} and Δn depend sensitively on temperature close to T_{AC} , and the electroclinic tilt [Figs. 8(a) and 8(c) and Figs. 9(a) and 9(c)] observed in the SmA^* phase is accompanied by the variation in the magnitude of Δn [Figs. 8(a) and 8(b) and Figs. 9(a) and 9(b)]. Based on the temperature and electric-field dependences of θ_{app} and Δn , we conclude that the SmA^* phase in both **DR276** (Fig. 8) and **DR277** (Fig. 9) is of the de Vries type [32–35], and the behavior of θ_{app} and Δn can be explained in terms of the de Vries diffuse cone model [10,23,36].

The spontaneous polarization P_S plots for **DR276** and **DR277** are shown in Fig. 10. Measurements are carried out on planar-aligned cells for cell thicknesses of 2.657 and 2.33 μm , respectively. Values of P_S were obtained by integrating the observed current peaks recorded under the application of triangular wave voltage [37,38]. To ensure that the polarization is saturated by the field, the amplitude of the triangular wave was selected for each sample at a maximum possible value without causing an irreversible damage to the sample (14.4 V/ μm for

DR276 and 7 V/ μm for **DR277**). The frequency of the waveform is optimized in SmA^* phase to minimize the hysteresis arising from the viscosity and ionic effects (81.7 Hz for **DR276** and 44 Hz for **DR277**). At $T = T_{AC} - 30^\circ\text{C}$, P_S for **DR276** is $\sim 80 \text{ nC cm}^{-2}$ and is $\sim 66 \text{ nC cm}^{-2}$ for **DR277**.

C. X-ray diffraction studies

The XRD patterns of **DR276** in Figs. 11(a)–11(c) show a pair of sharp arcs in the small-angle scattering region corresponding to the smectic-layer spacing and diffuse arcs for wide-angle scattering at 4.6 \AA corresponding to the effective molecular width. The pair of arcs are orthogonal to each other in the SmA^* phase [Fig. 11(a)] as indicated by the orthogonal solid yellow lines confirming an oriented domain in the SmA^* phase. At $T = 67.3^\circ\text{C}$, Fig. 11(b), the arcs became wider. However, upon a closer inspection, the arcs split azimuthally into several reflections for the same scattering position. This indicates tilting of the layer domains confirming the tilted SmC^* phase. Because of the multiple domains, it is not possible to determine quantitatively the tilt of the molecule with respect to the smectic layer. In the low-temperature mesophase below SmC^* [$T = 49.5^\circ\text{C}$, Fig. 11(c)] assigned here as SmX , arcs appear as rings. This is consistent with diffraction patterns observed for multiple unoriented smectic domains.

The temperature dependence of the layer spacing of **DR276**, plotted in Fig. 11(d), reflects the sample undergoing a weakly first-order phase transition to the SmC^* phase at $T = 78.5^\circ\text{C}$,

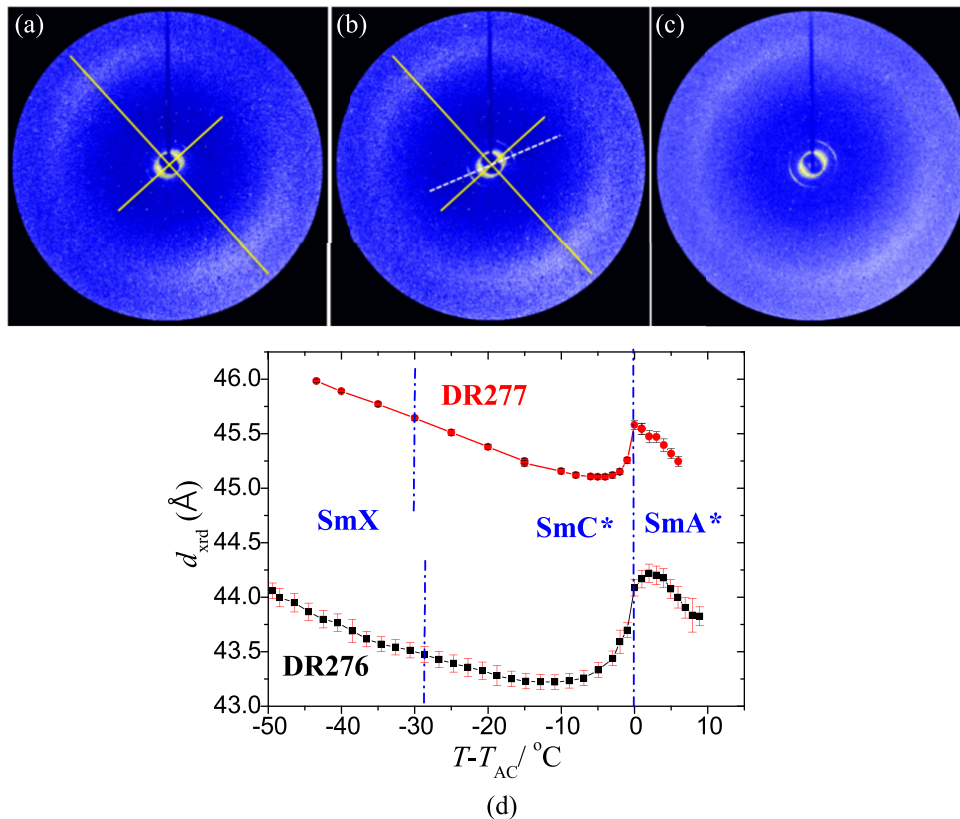


FIG. 11. X-ray diffraction patterns for **DR276** at temperatures (a) 80.1 $^\circ\text{C}$, (b) 67.3 $^\circ\text{C}$, and (c) 49.5 $^\circ\text{C}$. (d) Temperature dependence of the smectic-layer spacings for **DR276** and **DR277**. Note a reversal in the trend of the layer thickness from increasing to decreasing within the temperature range of SmA^* phase.

TABLE II. Properties of **DR276** and **DR277** compounds.

Properties	LC Materials	
	DR276	DR277
Iso-SmA* transition temperature	~87 °C	~77 °C
SmA* temperature range	~8.5 °C	~12.5 °C
SmA*-SmC* transition enthalpy (ΔH)	~0.4 J/g	~0.4 J/g
Δn at T_{AC} for $E = 0$	~0.059	~0.048
Δn at T_{AC} for $E = E_{\max}$	~0.078 (at 14.5 V/ μm)	~0.063 (at 7 V/ μm)
Difference in Δn at T_{AC}	0.019	0.015
θ_{app} at $T_{AC} + 0.2$ °C	~26.6° (at 14.5 V/ μm)	~26.1° (at 7 V/ μm)
Layer shrinkage at $T_{AC} - 10$ °C	~1.9%	~0.9%
Reduction factor, R at $T_{AC} - 10$ °C	~0.319	~0.222
P_S at $T_{AC} - 30$ °C	~80 nC/cm ² (at 14.5 V/ μm)	~67 nC/cm ² (at 7 V/ μm)

as indicated by a vertical blue dashed line at $T - T_{AC} = 0$. At the SmA*-SmC* phase transition, the layer spacing is $d_A = (44.09 \pm 0.05)$ Å. In the SmC* phase, the minimum layer spacing is $d_C = 43.23$ Å at $T = 68.5$ °C corresponding to $T = (T_{AC} - 10)$ °C. The optimal layer shrinkage, $\frac{d_A - d_C}{d_A} \times 100 = 1.9\%$, is minimal, which is one of the important characteristics of the de Vries smectics. The increasing layer spacing at temperatures below $T = 48$ °C could be interpreted as the untilting of the molecules back to the orthogonal state (i.e., molecules are perpendicular to the smectic layer). However, the observed optical texture [Fig. 7(g)] is not consistent with this interpretation, which means this phase remains in the tilted orientation. Notably, the maximum smectic layer spacing, 44.22 Å, is about 5 Å less than the molecular length ($L_{\text{calc}} = 49.71$ Å) in *all-trans* configuration as calculated using Avogadro (v1.1.1) [39].

The temperature dependence of the layer spacing of **DR277** is also shown in Fig. 11(d). Similar to **DR276**, a weakly first-order phase transition from SmA* to SmC* is observed at 65.5 °C. The maximum layer spacing occurs just above T_{AC} where $d_A = 45.58$ Å. The minimum layer spacing occurs at 10 °C below SmA* to SmC* $T = (T_{AC} - 10)$ °C, where $d_C = 45.16$ Å. The optimal layer shrinkage, $(d_A - d_C)/d_A \times 100 = 0.9\%$, is roughly one-half of the value obtained for **DR276**.

The reduction factor R , a measure of de Vriesness of a smectic LC, is defined as

$$R = \frac{\delta(T)}{\theta_{\text{app}}(T)} = \frac{\cos^{-1}[d_c(T)/d_{AC}]}{\theta_{\text{app}}(T)}, \quad (1)$$

where $\delta(T)$ determines the layer contraction relative to the layer spacing d_{AC} at the SmA* to SmC* transition temperature T_{AC} . This is based on the assumption that the rigid rod model of LCs is applicable to these materials [40]. θ_{app} is the apparent optical tilt angle determined using POM [Figs. 8(a) and 9(a)]. According to Eq. (1), the ideal de Vries smectic LC produces a defect-free bookshelf geometry in SmC* with $R = 0$, i.e., the short-range LC molecular tilt order at a lower temperature in the SmA* phase becomes long range close to the T_{AC} , where the de Vries cone angle is equal to the saturated θ_{opt} at $T = T_{AC}$. Upon entering the SmC*, the azimuthal ordering of the molecular director on the cone localizes these to a single orientation. In this case, the layer contraction is absent and then $d_c(T)/d_{AC} = 1$, and $R = 0$. The lowest reported magnitude of

reduction factor, R , is 0.17 for the chiral de Vries **QL32-6** LC, which exhibits a maximum layer contraction of only 0.2% at 3 K ($T = T_{AC} - 3$ K) below the SmA*-SmC* transitions with θ_{opt} of 20° [18]. The molecular design of **QL32-6** combines a tri-carbosilane end group attached to a 5-phenylpyrimidine core. Even though the **QL32-6** compound exhibits the smallest layer shrinkage, its crystallization temperature is approximately 53 °C and the SmC* phase is observed only over a temperature range of ~9 °C. In our case, **DR276** and **DR277** exhibit approximately 30 °C-wide SmC* phase regions and their crystallization temperatures are below 15 °C. Materials **DR276** and **DR277** at 10 °C below the SmA*-SmC* transition temperature T_{AC} ($T = T_{AC} - 10$ °C) lead to $R \approx 0.319$ and $R \approx 0.222$ and to the apparent optical tilt angles θ_{app} of 34.6° [Fig. 8(a)] and 35.1° [Fig. 9(a)], respectively. For **DR277**, the R value obtained is reasonably low and hence we can safely conclude that **DR277** is one of the “best de Vries smectic” LC.

Table II draws a comparison between the properties of **DR276** and **DR277** compounds.

IV. CONCLUSIONS

The objective of our current study is to explore new “excellent de Vries LCs,” and in order to advance our objective, new materials with a proposed strategy have been designed and characterized. The use of various techniques such as POM, XRD, and electro-optics including measurements of birefringence confirm that these compounds indeed have characteristics of de Vries smectics. Here, we report on the synthesis and de Vries properties of a 5-phenylpyrimidine benzoate mesogen terminated with a carbosilane tail on one side and the chiral 2-octanol on the opposite side. The techniques of DSC and POM are employed to determine the mesophase transition temperatures, the individual phases, and to find the phase-transition enthalpies. Measurements of the temperature-dependent smectic-layer spacing combined with results of θ_{app} and Δn reveal that the SmA* phase in these compounds is indeed of the de Vries type. A comparison of the two materials under study shows that the compound **DR277** with a tetra-carbosilane backbone exhibits better de Vries properties. We also show that by increasing the length of the carbosilane tail, the layer shrinkage from ~1.9% (for tri-carbosilane **DR276**) is reduced to ~0.9% (for tetra-carbosilane **DR277**). Our future work will involve synthesis of chiral mesogen similar to those

reported here but involving even higher numbers of carbosilane groups to optimize the excellent de Vries properties observed over a wide temperature range of the SmC* phase that also includes the ambient temperature. The carbosilane compounds introduced here exhibit almost ideal de Vries characteristics, as do the siloxane compounds studied extensively in the literature [41–43]. However, the carbosilane compounds are relatively more stable than siloxanes over time, and they are easily alignable.

ACKNOWLEDGMENTS

This research work was supported by 13/US/I2866 from the Science Foundation Ireland as part of the U.S.–Ireland Research and Development Partnership program jointly administered with the U.S. National Science Foundation under Grant No. NSF-DMR-1410649. Financial support for the Belfast group was from the Department for Employment and Learning under Grant Code USI 056.

-
- [1] N. A. Clark and S. T. Lagerwall, *Appl. Phys. Lett.* **36**, 899 (1980).
- [2] S. T. Lagerwall, *Ferroelectric and Antiferroelectric Liquid Crystals* (Wiley-VCH, Weinheim, 1999).
- [3] T. P. Rieker, N. A. Clark, G. S. Smith, D. S. Parmar, E. B. Sirota, and C. R. Safinya, *Phys. Rev. Lett.* **59**, 2658 (1987).
- [4] J. P. F. Lagerwall and F. Giesselmann, *Chem. Phys. Chem.* **7**, 20 (2006).
- [5] S. Diele, P. Brand, and H. Sackmann, *Mol. Cryst. Liq. Cryst.* **16**, 105 (1972).
- [6] A. de Vries, *Mol. Cryst. Liq. Cryst.* **41**, 27 (1977).
- [7] A. de Vries, A. Ekachai, and N. Spielberg, *Mol. Cryst. Liq. Cryst. Lett.* **49**, 143 (1979).
- [8] A. de Vries, *J. Chem. Phys.* **71**, 25 (1979).
- [9] S. Garoff and R. B. Meyer, *Phys. Rev. Lett.* **38**, 848 (1977).
- [10] S. P. Sreenilayam, D. M. Agra-Kooijman, V. P. Panov, V. Swaminathan, J. K. Vij, Yu. P. Panarin, A. Kocot, A. Panov, D. Rodriguez-Lojo, P. J. Stevenson, M. R. Fisch, and S. Kumar, *Phys. Rev. E* **95**, 032701 (2017).
- [11] N. Yadav, V. P. Panov, V. Swaminathan, S. P. Sreenilayam, J. K. Vij, T. S. Perova, R. Dhar, A. Panov, D. Rodriguez-Lojo, and P. J. Stevenson, *Phys. Rev. E* **95**, 062704 (2017).
- [12] H. Xu, J. K. Vij, A. Rappaport, and N. A. Clark, *Phys. Rev. Lett.* **79**, 249 (1997); Yu. P. Panarin, H. Xu, S. T. MacLughadha, and J. K. Vij, *Jap. J. Appl. Phys.* **33**, 2648 (1994).
- [13] U. Manna, J.-K. Song, Yu. P. Panarin, A. Fukuda, and J. K. Vij, *Phys. Rev. E* **77**, 041707 (2008).
- [14] J. P. F. Lagerwall, F. Giesselmann, and M. D. Radcliffe, *Phys. Rev. E* **66**, 031703 (2002).
- [15] M. S. Spector, P. A. Heiney, J. Naciri, B. T. Weslowski, D. B. Holt, and R. Shashidhar, *Phys. Rev. E* **61**, 1579 (2000).
- [16] H. G. Yoon, D. M. Agra-Kooijman, K. Ayub, R. P. Lemieux, and S. Kumar, *Phys. Rev. Lett.* **106**, 087801 (2011).
- [17] D. M. Agra-Kooijman, H. G. Yoon, S. Dey, and S. Kumar, *Phys. Rev. E* **89**, 032506 (2014).
- [18] C. P. J. Schubert, C. Müller, F. Giesselmann, and R. P. Lemieux, *J. Mater. Chem. C* **4**, 8483 (2016).
- [19] J. C. Roberts, N. Kapernaum, Q. Song, D. Nonnenmacher, K. Ayub, F. Giesselmann, and R. P. Lemieux, *J. Am. Chem. Soc.* **132**, 364 (2010).
- [20] V. Swaminathan, V. P. Panov, Yu. P. Panarin, S. P. Sreenilayam, J. K. Vij, A. Panov, D. Rodriguez-Lojo, P. J. Stevenson, and E. Gorecka, *Liq. Cryst.* (2017), doi: 10.1080/02678292.2017.1359694.
- [21] S. P. Sreenilayam, D. Rodriguez-Lojo, V. P. Panov, V. Swaminathan, J. K. Vij, Y. P. Panarin, E. Gorecka, A. Panov, and P. J. Stevenson, *Phys. Rev. E* **96**, 042701 (2017).
- [22] K. M. Mulligan, A. Bogner, Q. Song, C. P. J. Schubert, F. Giesselmann, and R. P. Lemieux, *J. Mater. Chem. C* **2**, 8270 (2014).
- [23] Y. Shen, L. Wang, R. Shao, T. Gong, C. Zhu, H. Yang, J. E. MacLennan, D. M. Walba, and N. A. Clark, *Phys. Rev. E* **88**, 062504 (2013).
- [24] Y. Zhang, U. Baumeister, C. Tschierske, M. J. O’Callaghan and C. Walker, *Chem. Mater.* **22**, 2869 (2010).
- [25] <http://www.linkam.co.uk/system-control-software/>.
- [26] A. P. Hammersley, S. O. Svensson, M. Hanfland, A. N. Fitch, and D. Hausermann, *High Press. Res.* **14**, 235 (1996).
- [27] G. W. Gray and J. W. Goodby, *Smectic Liquid Crystals* (Leonard Hill, London, 1984).
- [28] D. Nonnenmacher, M. A. Osipov, J. C. Roberts, R. P. Lemieux, and F. Giesselmann, *Phys. Rev. E* **82**, 031703 (2010); A. Kocot, R. Wrzalik, J. K. Vij, M. Brehmer, and R. Zentel, *Phys. Rev. B* **50**, 16346 (1994).
- [29] J. W. Goodby, P. J. Collings, T. Kato, C. Tschierske, H. F. Gleeson, and P. Raynes, *Handbook of Liquid Crystals*, 2nd ed. (Wiley-VCH, Weinheim, 2014), Vol. 1, Chap. 3.
- [30] B. Park, S.-S. Seomun, M. Nakata, M. Takahashi, Y. Takahashi, K. Ishikawa, and H. Takezoe, *Jpn. J. Appl. Phys.* **38**, 1474 (1999).
- [31] S. T. Lagerwall, P. Rudquist, and F. Giesselmann, *Mol. Cryst. Liq. Cryst.* **510**, 148 (2009).
- [32] J. V. Selinger, P. J. Collings, and R. Shashidhar, *Phys. Rev. E* **64**, 061705 (2001).
- [33] O. E. Panarina, Yu. P. Panarin, F. Antonelli, J. K. Vij, M. Reihmann, and G. Galli, *J. Mater. Chem.* **16**, 842 (2006).
- [34] Yu. P. Panarin, V. Panov, O. E. Kalinovskaya, and J. K. Vij, *J. Mater. Chem.* **9**, 2967 (1999).
- [35] A. Kocot, J. K. Vij, T. S. Perova, K. Merkel, V. Swaminathan, S. P. Sreenilayam, N. Yadav, V. P. Panov, P. J. Stevenson, A. Panov, and D. Rodriguez-Lojo, *J. Chem. Phys.* **147**, 094903 (2017).
- [36] N. A. Clark, T. Bellini, R.-F. Shao, D. Coleman, S. Bardou, D. R. Link, J. E. MacLennan, X.-H. Chen, M. D. Wand, D. M. Walba, P. Rudquist, and S. T. Lagerwall, *Appl. Phys. Lett.* **80**, 4097 (2002).
- [37] K. Miyasato, S. Abe, H. Takezoe, A. Fukuda, and E. Kuze, *Jpn. J. Appl. Phys.* **22**, L661 (1983).
- [38] G. Spruce and R. D. Pringle, *J. Phys. E* **21**, 268 (1988).
- [39] M. D. Hanwell, D. E. Curtis, D. C. Lonie, T. Vandermeersch, E. Zurek, and G. R. Hutchison, *J. Cheminformatics* **4**, 17 (2012).
- [40] Y. Takahashi, Y. Ouchi, H. Takezoe, A. Fukuda, A. Mochizuki, and M. Nakatsuka, *Jpn. J. Appl. Phys.* **29**, L984 (1990).

- [41] N. Hayashi, T. Kato, A. Fukuda, J. K. Vij, Yu. P. Panarin, J. Naciri, R. Shashidhar, S. Kawada, and S. Kondoh. *Phys. Rev. E* **71**, 041705 (2005).
- [42] O. E. Panarina, Yu. P. Panarin, J. K. Vij, M. S. Spector, and R. Shashidhar, *Phys. Rev. E* **67**, 051709 (2003).
- [43] A. Kocot, R. Wrzalik, J. K. Vij, and R. Zentel, *J. Appl. Phys.* **75**, 728 (1994).
- [44] See Supplemental Material at <http://link.aps.org/supplemental/10.1103/PhysRevMaterials.2.025603> for additional information on synthetic details, purity tests and verification.